Materials Advances

PAPER

Check for updates

Electronic structure of Li⁺@C₆₀ adsorbed on methyl-ammonium lead iodide perovskite CH₃NH₃PbI₃ surfaces†

Khian-Hooi Chew, [ID] *[a] Riichi Kuwahara [ID] [b] and Kaoru Ohno [ID] [c]

It was recently shown by Jeon et al. [Angew. Chem., 2018, **57**, 4607] that air stability for more than 1000 hours under light illumination can be achieved in methyl-ammonium (MA) lead iodide perovskite solar cells when Li⁺ is replaced by Li⁺@C₆₀ in a dopant material used in the p-type donor layer. In order to demonstrate the role of Li⁺@C₆₀ in the hole transporting material, we carried out first-principles electronic structure calculations of Li⁺@C₆₀ adsorbed on MAPbI₃ using the van der Waals corrected density functional theory. We used finite slab models of tetragonal MAPbI₃ (001) surfaces with MAI terminations. Using the most stable MAPbI₃ surfaces, we introduced one Li⁺@C₆₀ molecule on various positions of the MAI surface and performed geometrical optimizations. Then, we found that the Li⁺@C₆₀ was adsorbed at the aboveC position with almost 100% ionization. There is not much difference between the top and bottom positions of Li⁺ inside C₆₀, but the bottom position is slightly more stable than the top position. In the MAPbI₃/Li⁺@C₆₀ system, the Kohn–Sham (KS) wave functions of the HOMO and HOMO-1 levels are spread out in MAPbI₃ and those of the LUMO, LUMO+1, LUMO+2 levels are localized in Li⁺@C₆₀; the energy gap between these levels is 0.6 eV. Thus, in the neutral, spin-polarized MAPbI₃/Li@C₆₀ system, the KS wave functions of the HOMO (SOMO, − spin) and LUMO (+spin) levels are both localized in Li@C₆₀ and their energy gap of 0.125 eV is very small. This HOMO (SOMO) level behaves as a hole level when it loses an electron to become Li⁺@C₆₀. Since there are three almost degenerate LUMO+1 and LUMO+2 levels, it is expected to behave as a good hole conductor. As such, we conclude that the use of Li⁺@C₆₀ molecules in place of the bare Li-ions as dopant materials in the MAPbI₃ solar cells can prevent degradation. In any case, regardless of the adsorption geometry, our results clearly show the existence of the energetically isolated hole level localized in the Li@C₆₀, which may successfully contribute to the suppression of the oxidation of the MAPbI₃ surface.

Introduction

Methylammonium (MA) lead halide perovskites such as CH₃NH₃PbI₃ (hereafter abbreviated to MAPbI₃) have attracted significant attention since the discovery of the efficient photovoltaic behaviour of the heterojunction of MAPbI₃ and TiO₂ by Miyasaka's group in 2009.[1–3] So far, various heterojunction systems overlaid with SnO₂, C₆₀, C₆₀ derivatives like PCBM, and so on have been proposed by many researchers, and the light-current energy conversion efficiency has rapidly increased from 3.8%[1] to over 20%.[3–7] In a typical architecture of perovskite solar cells (PSCs), MAPbI₃ works as a photoabsorber and is sandwiched by an n-type acceptor layer and a p-type donor layer. The former is made of electron transporting material (ETM) such as C₆₀ and C₆₀ derivatives and the latter is made of hole transporting material (HTM) such as 2,2′,7,7′-tetrakis(N,N-di-p-methoxyphenylamine)-9,9′-spirobi-fluorene (spiro-MeOTAD) and poly(3,4-ethylenedioxythiophene) polystyrene sulfonate (PEDOT:PSS).[2,8–11]

Although the application of Spiro-MeOTAD as an HTM in PSCs[2,12] has been an important step in improving the energy conversion efficiency, the low long-term stability under light illumination and the coexistence of oxygen and water have been serious drawbacks of PSCs for commercial use.[13–15] In particular, the dopants used in the HTM suffer from degradation.[13–17] In order to reduce degradation, Jeon et al.[18] proposed the use of Li-ion encapsulated C₆₀ (Li⁺@C₆₀) instead of bare Li-ions (Li⁺) in combination with bis(trifluoromethanesulfonyl)imide (TFSI⁻) as a p-type dopant. Using this dopant, they reported

ᵃ Department of Physics, University of Malaya, 50603 Kuala Lumpur, Malaysia.
  E-mail: khchew@um.edu.my
ᵇ Dassault Systèmes, ThinkPark Tower, 2-1-1 Osaki, Shinagawa-ku, Tokyo 141-6020,
  Japan
ᶜ Department of Physics, Yokohama National University, 79-5 Tokiwadai,
  Hogogaya-ku, Yokohama 240-8501, Japan
† Electronic supplementary information (ESI) available. See DOI: 10.1039/d1ma00741f

that spiro-MeOTAD$^{\bullet+}$TFSI$^-$ functions as an effective HTM and Li$^+$@C$_{60}$ functions as an antioxidant, reacting with intruding oxygen. By preventing unnecessary oxidation in the device system, the [Li$^+$@C$_{60}$]TFSI$^-$ device achieved a stability of approximately 7-fold that of conventional Li$^+$TFSI$^-$ devices in MAPbI$_3$-based PSCs, and 10-fold that of a more stable mixed ion lead halide PSCs. Consequently, the passivated PSCs showed no decrease in the energy conversion efficiency for more than 1000 hours while being continuously illuminated under ambient conditions.

Atomistic modelling and simulation based on first-principles density functional theory (DFT) can play an important role in revealing the underlying mechanisms of the high performance of PSCs.[19–21] Yin et al.[22] studied the energy alignment and charge transfer properties at the interface between MAPbI$_3$ perovskites and Spiro-MeOTAD and PCBM. They found that the MAPbI$_3$ (001) and (110) surfaces favored hole injection to the hole acceptor Spiro-MeOTAD, whereas the polar MAPbI$_3$ (001) surface facilitated electron transfer to the PCBM. However, concerning the reduction of the degradation of PSCs, the role of Li$^+$@C$_{60}$ adsorbed on the MAPbI$_3$ surface in the experiment by Jeon et al.[18] remains unclear. Therefore, the purpose of this paper is to investigate the electronic structure of Li$^+$@C$_{60}$ adsorbed on the MAPbI$_3$ surface. The mass production of Li$^+$@C$_{60}$ was achieved by a plasma shower method,[23] which was suggested by a first-principles molecular dynamics study[24] and experiments.[25,26] The maximum production ratio in this method was theoretically estimated to be about 3.7%.[27] Now, Li$^+$@C$_{60}$ has the potential for many applications.[28–33]

Computational methods

First-principles all-electron calculations were performed by using the DMol^3 package,[34–36] which adopts numerical atomic orbitals. A standard DFT dispersion (DFT-D) correction was employed to take into account van der Waals interactions[37] in the Tkatchenko-Scheffler (TS) scheme.[38] This method is formally identical to the DFT-D2 method of Grimme but the dispersion coefficients and damping function are charge-density dependent. The DFT-TS method can therefore handle the change in the vdW contribution of atoms due to their chemical environment. In the present study, we considered a slab model of the tetragonal phase of MAPbI$_3$ (001) with MAI-terminated surfaces. The slab model has a 2 × 2 periodicity in-plane and is four MAI-layers thick, with the assumption of 50 Å vacuum regions between the slabs, which are large enough to avoid the interactions between periodic images. The MAPbI$_3$ slab model and endohedral Li$^+$@C$_{60}$ fullerene were first optimized to achieve the minimum energy. We introduced one Li$^+$@C$_{60}$ molecule on the MAPbI$_3$ (001) layer, forming a hybrid MAPbI$_3$/Li$^+$@C$_{60}$ structure with a total of 445 atoms. For the MAPbI$_3$/Li$^+$@C$_{60}$ interface, the dipole slab correction for the electrostatic potential was taken into account in the calculations due to the existence of polar bonds.

All calculations (except for perovskites with bare surfaces) were performed based on the spin unrestricted (i.e., spin-polarized) approach using the generalized gradient approximation (GGA) in the Perdew–Burke–Ernzerhof (PBE) form for the exchange–correlation functional.[39] We have ignored spin–orbit coupling (SOC) because the PBE functional can provide a reasonable estimation of structural, electronic, and optical properties.[40–42] The double-numerical quality basis, i.e., double numerical plus polarization (DNP) function, was employed for all calculations. The size of these DNP basis sets is comparable to that of the Gaussian 6-31G**. In the calculation, the geometrical optimization was performed with the Fermi smearing of 0.005 Hartree. The tolerances of the energy, gradient, and displacement convergences were set at 1×10^{-5} Ha, 2×10^{-3} Ha Å^{-1}, and 5×10^{-3} Å, respectively.

Results & discussion

MAPbI$_3$ undergoes a structural phase transition from a cubic to a tetragonal phase at ∼330 K, and it becomes an orthorhombic structure at temperatures below 160 K.[43] In the present study, the room temperature tetragonal phase of MAPbI$_3$ was chosen as the model structure for studying the structural and electronic properties in the Li@C$_{60}$ adsorbed geometries. The computationally optimized cell parameters for the bulk tetragonal phase of MAPbI$_3$ are $a = 8.70$ Å, $b = 8.72$ Å and $c = 12.83$ Å, which are comparable to experimental values.[43,44] A typical PSC has asymmetric interfaces ETM/MAPbI$_3$/HTM. Therefore, we consider an asymmetric slab model with the MAI as the top surface layer (facing the vacuum layer) and the PbI layer as the bottom layer of MAPbI$_3$. Here, the MAI-terminated surface is set as the MAPbI$_3$ top surface because this surface facilitates the electron transfer to the C$_{60}$ ETM.[45]

Many studies have shown that the MA orientation plays an important role in governing the stability and electronic structures of MAPbI$_3$.[7,42,45–48] The orientation of the MA molecule
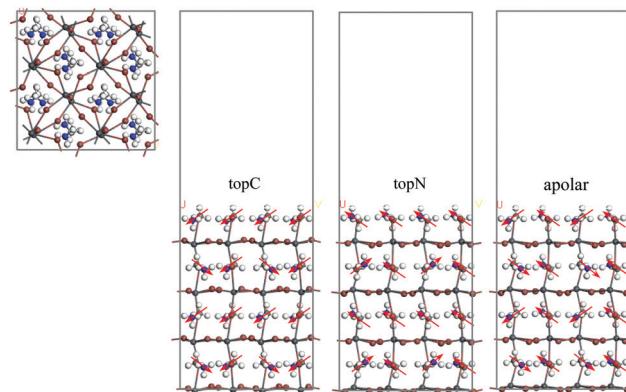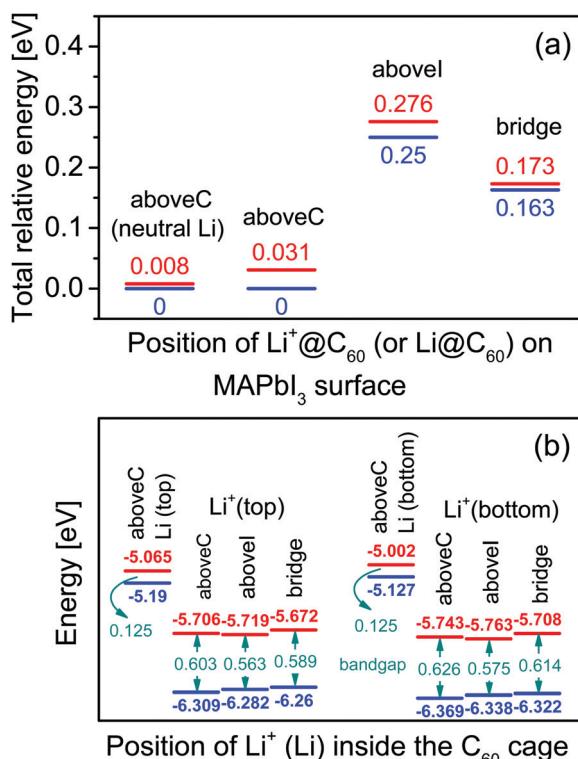
Fig. 1 Slab models constructed for the simulation of the MAPbI$_3$ (001) surfaces with MAI terminations: top and side views of tetragonal MAPbI$_3$ (001) surfaces for topC, topN and apolar geometries. The red arrows show the molecular dipole of a MA cation with the NH$_3$ group as the arrowhead. White, light grey, blue, brown, and dark grey spheres represent the H, C, N, I, and Pb atoms, respectively.

Table 1 Valence band edge (VBE), conductance band edge (CBE), band gap and the total relative energies of the bare-surface for tetragonal MAPbI$_3$ perovskites
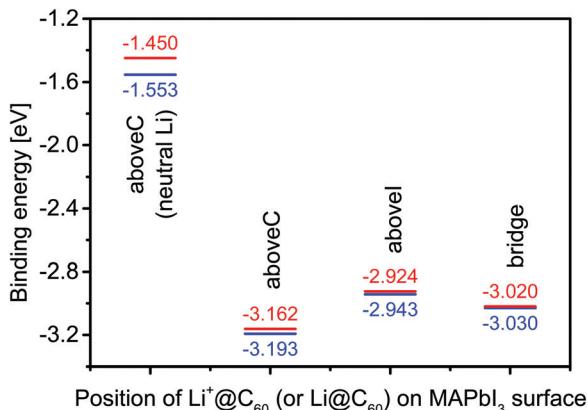
MA orientation	VBE [eV]	CBE [eV]	Band gap [eV]	Total energy relative to the topC [eV]
topC	−5.371	−3.888	1.482	0.00
topN	−4.644	−3.552	1.092	3.814
Apolar	−4.905	−3.619	1.286	2.505
Experiment			1.55[a]	

[a] Ref. 45.

Fig. 3 The binding energy of a tetragonal MAPbI$_3$ with a Li$^+$@C$_{60}$ (a Li@C$_{60}$). The Li$^+$ (Li) is located at the off-central top (━ red line) and bottom (━ blue line) positions inside the C$_{60}$ cage. The calculated binding energy of a MAPbI$_3$ with a neutral lithium endohedral fullerene Li@C$_{60}$ is only for the aboveC position.
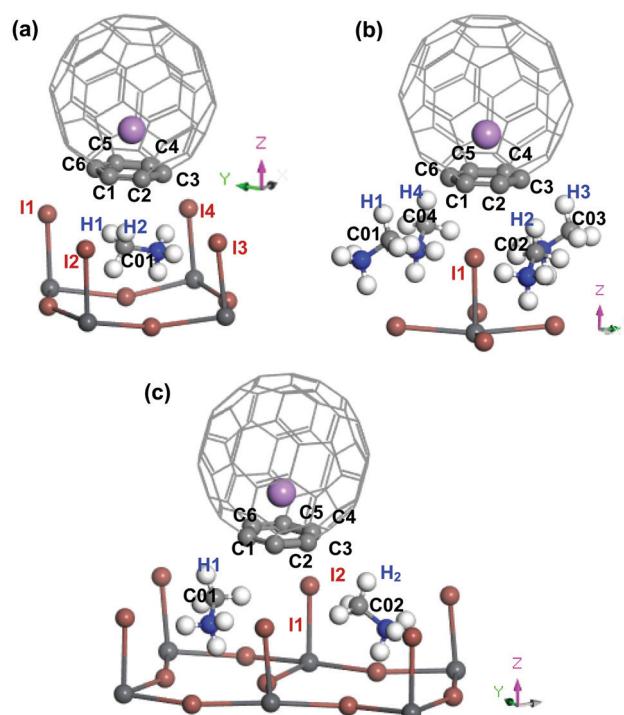
Fig. 2 (a) Total energy of a tetragonal MAPbI$_3$ with a Li$^+$@C$_{60}$ (a Li@C$_{60}$) relative to the aboveC position. The Li$^+$ (Li) is located at the off-central top (━ red line) and bottom (━ blue line) positions inside the C$_{60}$ cage. The total energy of a MAPbI$_3$ with a neutral lithium endohedral fullerene Li@C$_{60}$ was calculated only for the aboveC position. (b) The highest occupied molecular orbital (━ HOMO), lowest unoccupied molecular orbital (━ LUMO) and band gap of the tetragonal MAPbI$_3$ with a Li$^+$@C$_{60}$ on the aboveC, abovel, and bridge positions. The MAPbI$_3$ with a neutral lithium endohedral fullerene Li@C$_{60}$ was calculated only for the aboveC position.

cation with respect to the top surface as shown in Fig. 1: (i) the topC model with the CH$_3$ group pointing up in all layers, (ii) the topN model with the NH$_3$ group pointing up in all layers, and (iii) the apolar model with half of –NH$_3$ or –CH$_3$ groups

Fig. 4 Perspective view (only selected area at the interface between MAPbI$_3$ and Li$^+$@C$_{60}$) of the topC-oriented MAPbI$_3$ with a lithium endohedral fullerene Li$^+$@C$_{60}$ on the (a) aboveC, (b) abovel and (c) bridge position. The Li$^+$ is located at the off-central bottom inside the C$_{60}$ cage. H, C, N, I, Pb and Li atoms are represented by the white, light grey, blue, brown, dark grey and purple spheres, respectively. Atoms located at the interface between MAPbI$_3$ and C$_{60}$ are labelled, and their atomic distances within the estimated vdWs atomic radius are summarized in Table 2.

has a significant effect on the charge mobility,[46] the bandgap change[47] and photo-energy conversion efficiencies.[7,48] Neutron scattering measurements suggested the formation of either antiferroelectric or ferroelectric domains in these perovskites based on the ordered orientation of MA cations.[48] However, the highly disordered orientation of the MA cation at room temperature excludes the possibility of spontaneous polarization in the antiferroelectrics or ferroelectrics due to the ordered orientation of MA cations. In order to take into account the MA orientation effect, we considered three orientations of the MA

pointing up and half pointing down. We first looked at the energetics of the slab models. In Table 1, we summarize the valence band edge (VBE), conductance band edge (CBE), band gap, and the total relative energies of the tetragonal $MAPbI_3$ perovskites with the bare surface. The calculated VBE and CBE for the bare-surface tetragonal $MAPbI_3$ were -4.66 to -5.37 eV and -3.55 to -3.88 eV, respectively. Among them, the topC orientation was the most stable structure with the bandgap of 1.48 eV, in agreement with other works.[49] Since the topC model is the most stable structure, we will focus on the tetragonal $MAPbI_3$ perovskites with the topC orientation by introducing a $Li^+@C_{60}$ molecule on various $MAPbI_3$ surfaces: the aboveC, aboveI and bridge positions (see Fig. S1–S3 of the ESI†). In each case, we examined the effect of the Li^+ located at the off-central top and bottom inside the C_{60} cage on the electronic structures of the $MAPbI_3/Li^+@C_{60}$ system. Hereafter, we denote the $Li^+(top)@C_{60}$ and $Li^+(bottom)@C_{60}$ molecules as the lithium-ion endohedral fullerene with the Li^+ located at the off-central "top" and "bottom" inside the C_{60} cage, respectively.

Using the most stable topC model, we introduced one $Li^+@C_{60}$ molecule on the aboveC, aboveI and bridge positions of the MAI surface and performed geometrical optimizations. Fig. 2(a) shows the total energy of the $MAPbI_3/Li^+@C_{60}$ system relative to the case with a $Li^+(bottom)@C_{60}$ on the aboveC geometry. The corresponding HOMO, LUMO and band gap are shown in Fig. 2(b). The binding energy of the $MAPbI_3/Li^+@C_{60}$ system for three different geometries and the binding energy of the $MAPbI_3/Li@C_{60}$ system for the aboveC geometry are shown in Fig. 3. In general, the stability of the $MAPbI_3/Li^+@C_{60}$ system is in the order of a $Li^+@C_{60}$ on the aboveC > bridge > aboveI position. From Fig. 3, the binding energy of the $MAPbI_3/Li@C_{60}$ system also increased in the order of a $Li^+@C_{60}$ on the aboveC > bridge > aboveI geometry, which further confirmed the stability of the $MAPbI_3/Li^+@C_{60}$ system. In addition, the $MAPbI_3/Li^+(bottom)@C_{60}$ system is energetically more stable than the $MAPbI_3/Li^+(top)@C_{60}$ system for the same geometry (see Fig. 2(a)), which is also consistent with the binding energies of the $MAPbI_3/Li^+@C_{60}$ system

Table 3 Hirshfeld atomic charges of fragments [CH₃] and [1] at the $MAPbI_3/Li^+@C_{60}$ interface with the $Li^+@C_{60}$ on the aboveC, aboveI and bridge positions. $[Li^+@C_{60}]$ and $[MAPbI_3]$ denote the calculated Hirshfeld fragments of the $MAPbI_3/Li^+@C_{60}$ system. Q is the charge transferred from $[MAPbI_3]$ to $[Li^+@C_{60}]$. The Li^+ is located at the off-central top ($Li^+/Li(top)$) and bottom ($Li/Li^+(bottom)$) inside the C_{60} cage. Fragments [CH₃] and [1] are labelled according to Fig. 4. Calculated Hirshfeld atomic charges of a $MAPbI_3$ with a neutral lithium endohedral fullerene $Li@C_{60}$ are for only the aboveC position

Atom/ molecule	Surface geometry					
	aboveC [e]		aboveI [e]		Bridge [e]	
	Li (top)	Li (bottom)	Li^+ (top)	Li^+ (bottom)	Li^+ (top)	Li^+ (bottom)
$[C01H_3]$	−0.004	−0.007	0.057	0.058	0.058	0.057
[1]	−0.205	−0.211	−0.169	−0.177	−0.213	−0.218
$[Li^+@C_{60}]$	0.208	0.239	0.245	0.271	0.248	0.278
$[MAPbI_3]$	0.789	0.758	0.752	0.726	0.745	0.715
$MAPbI_3/Li^+@C_{60}$	0.997	0.997	0.997	0.997	0.993	0.994
Q	−0.794	−0.763	−0.757	−0.731	−0.750	−0.720
$[C01H_3]$	−0.006	−0.007				
[1]	−0.212	−0.211				
$[Li@C_{60}]$	−0.049	−0.067				
$[MAPbI_3]$	0.046	0.064				
$MAPbI_3/Li@C_{60}$	−0.003	−0.003				
Q	−0.051	−0.069				

((see Fig. 3)). Although iodine has a high electronegativity, a $Li^+@C_{60}$ adsorbed on the aboveI position of the $CH_3NH_3PbI_3$ surface is energetically less favorable as compared to other geometries. Among the $MAPbI_3/Li^+@C_{60}$ systems, a $Li^+(bottom)@C_{60}$ absorbed on the aboveC geometry of the $MAPbI_3$ surface is the most stable structure with the strongest binding energy of -3.193 eV (Fig. 3) and the highest bandgap value of 0.626 eV (Fig. 2(b)).

For the $MAPbI_3/Li^+(bottom)@C_{60}$ system, the LUMO varies from -5.708 eV to -5.763 eV and the HOMO has a value range from -6.322 eV to -6.369 eV, leading to a bandgap value in the range from 0.575 eV to 0.626 eV. Compared with the $MAPbI_3/Li^+(bottom)@C_{60}$ system, the $MAPbI_3/Li^+(top)@C_{60}$ system has

Table 2 Atomic distances of selected atoms located within the vdWs atomic radius at the $MAPbI_3/Li^+@C_{60}$ interface with the $Li^+@C_{60}$ on the aboveC, aboveI and bridge positions. Calculated atomic distances at the interface between the $MAPbI_3$ and a neutral Li endohedral fullerene $Li@C_{60}$ are for only the aboveC position. The Li^+/Li is located at the off-central top inside the C_{60} cage. Values in brackets denote the atomic distance for the Li^+/Li located at the off-central bottom inside the C_{60} cage. Atoms are labelled according to Fig. 4

| Surface geometry	C···H distance [Å] [vdWs radius <2.97 Å]		C···C distance [Å] [vdWs radius <3.54 Å]		C···I distance [Å] [vdWs radius <3.81 Å]	
aboveC (neutral Li)	C5···H1	— (2.944)				
	C1···H2	2.672 (2.967)	C1···C01	3.547 (3.538)	C4···I4	3.782 (3.744)
	C2···H2	2.621 (2.618)	C2···C01	3.545 (3.544)		
	C3···H2	2.973 (—)				
aboveC	C1···H2	2.665 (2.660)	C1···C01	3.544 (3.538)	C4···I4	3.787 (3.744)
	C2···H2	2.619 (2.612)	C2···C01	(3.544)		
aboveI					C1···I1	3.411 (3.428)
					C2···I1	3.566 (3.580)
					C3···I1	3.742 (3.742)
					C4···I2	3.762 (3.751)
					C5···I2	3.613 (3.604)
					C6···I2	3.438 (3.442)
bridge	C6···H1	2.801 (2.791)	C6···C01	3.457 (3.443)	C2···I1	3.568 (3.519)
	C3···H2	2.990 (2.974)	C3···C02	3.465 (3.451)	C5···I2	3.741 (3.703)
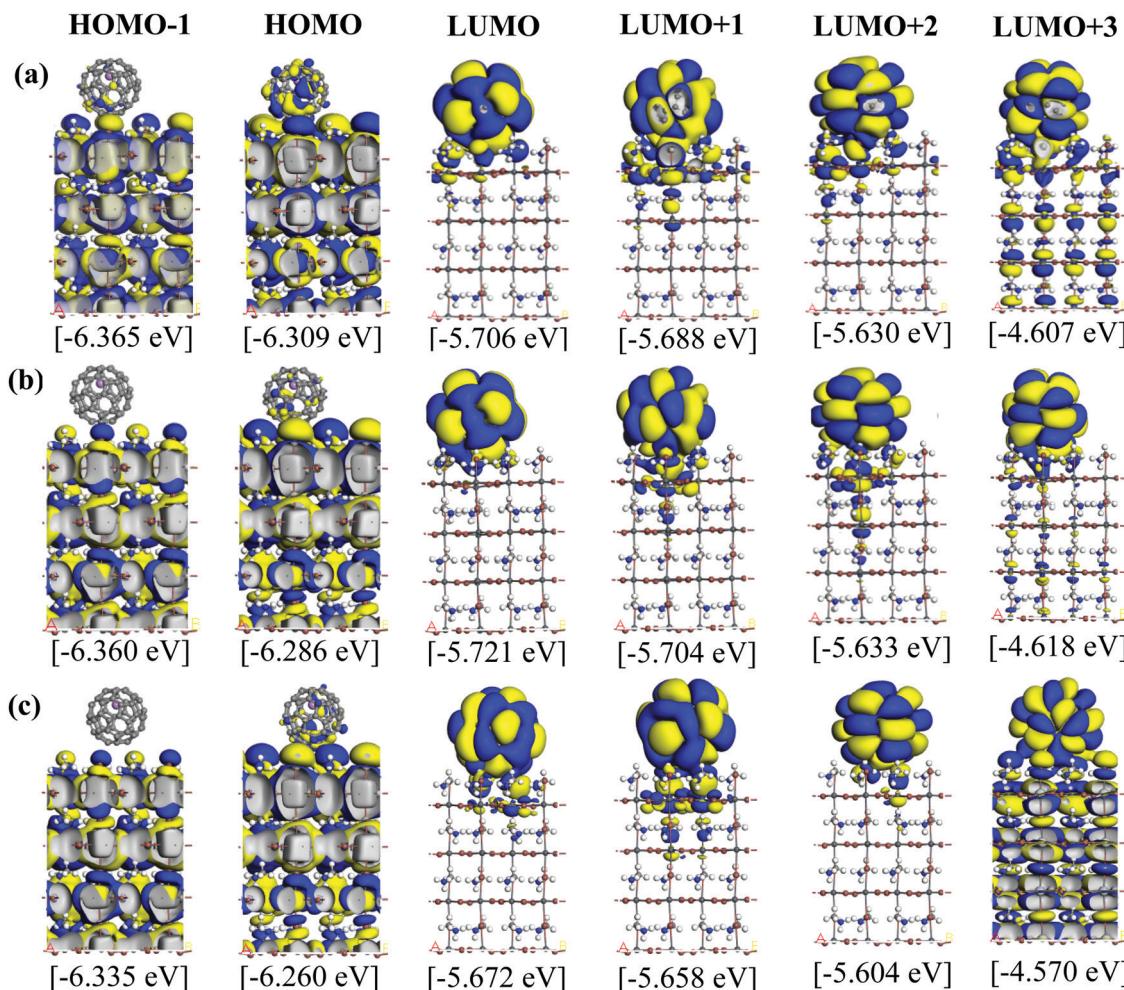
Fig. 5 Calculated KS orbitals and energy eigenvalues of $MAPbI_3/Li^+@C_{60}$ from the HOMO−1 to LUMO+3 levels. The Li^+ is located at the off-central top inside the C_{60} cage. Yellow and blue denote the plus and minus regions of the orbitals. The perovskite has a topC orientation with $Li^+@C_{60}$ on the (a) aboveC, (b) aboveI and (c) bridge positions.

a slightly lower bandgap ranging from 0.563 eV to 0.603 eV; the LUMO varies from −5.672 eV to −5.706 eV and the HOMO varies from −6.260 to −6.309 eV. It is interesting to note here that the $MAPbI_3/Li^+@C_{60}$ system with the aboveC (aboveI) geometry has the largest (smallest) bandgap value of 0.603 (0.563) eV and 0.626 (0.575) eV for the Li^+ located at the off-central "top" and "bottom" inside the C_{60} cage, respectively.

Since the $MAPbI_3/Li^+@C_{60}$ system with the aboveC geometry is the most stable structure, we calculated and compared the electronic structures of the $MAPbI_3/Li^+@C_{60}$ system with a neutral lithium endohedral fullerene $Li@C_{60}$ absorbed on the aboveC geometry of the $MAPbI_3$ surface ($MAPbI_3/Li@C_{60}$). The total energy relative to the $MAPbI_3/Li(bottom)@C_{60}$ with the aboveC geometry is depicted in Fig. 2(a), which is very small, *i.e.* ∼0.008 eV, compared to the $MAPbI_3/Li^+@C_{60}$ system. Since the binding energy of the $MAPbI_3/Li@C_{60}$ system is smaller than that of the $MAPbI_3/Li^+@C_{60}$ system by over 1.5 eV as shown in Fig. 3, $Li@C_{60}$ has a great tendency to become a good hole conductor by absorbing a hole. From Fig. 2(b), it is seen that the $MAPbI_3/Li(top)@C_{60}$ has a small band gap of 0.125 eV, which is

independent of the off-central position of Li and is smaller than the bandgap of the $MAPbI_3/Li^+@C_{60}$ system by a factor of 5. The LUMO and HOMO (SOMO) of the $MAPbI_3/Li@C_{60}$ system are ∼−5.0 eV and ∼−5.1 eV, respectively, which are relatively higher than those of the $MAPbI_3/Li^+@C_{60}$ system (see Fig. 7).

When two atoms with opposite charges from two molecular species are in proximity within the sum of their van der Waals (vdW) radii, a non-covalent intermolecular interaction may form between the molecules.[50–52] At the interface between the $Li^+@C_{60}$ (or the $Li@C_{60}$) molecule and the topC-oriented $MAPbI_3$, the C atoms of C_{60} may interact with the $MAPbI_3$ surface *via* the I atoms of PbI_3 and H (or C) atoms of MA, as shown in Fig. 4 and Fig. S4–S11 (ESI†). The vdW radii of C, H, and I are 1.77 Å, 1.20 Å, and 2.04 Å, respectively.[53] This indicates that any C···H(–C) distance < 2.97 Å, C···C(–H3) distance < 3.54 Å, or C···I(–Pb) distance < 3.81 Å may signify a potential interaction between the $Li^+@C_{60}$ and $MAPbI_3$ surface. Based on this criterion, we conducted a simple analysis of the interactions at the $MAPb_3I/Li^+@C_{60}$ interface for three different geometries. We also examined the $MAPbI_3/Li@C_{60}$ system with

| | HOMO−1 | HOMO | LUMO | LUMO+1 | LUMO+2 | LUMO+3 |

(a) [−6.425 eV] [−6.369 eV] [−5.743 eV] [−5.722 eV] [−5.648 eV] [−4.629 eV]

(b) [−6.416 eV] [−6.347 eV] [−5.768 eV] [−5.744 eV] [−5.653 eV] [−4.639 eV]

(c) [−6.388 eV] [−6.322 eV] [−5.708 eV] [−5.691 eV] [−5.628 eV] [−4.622 eV]
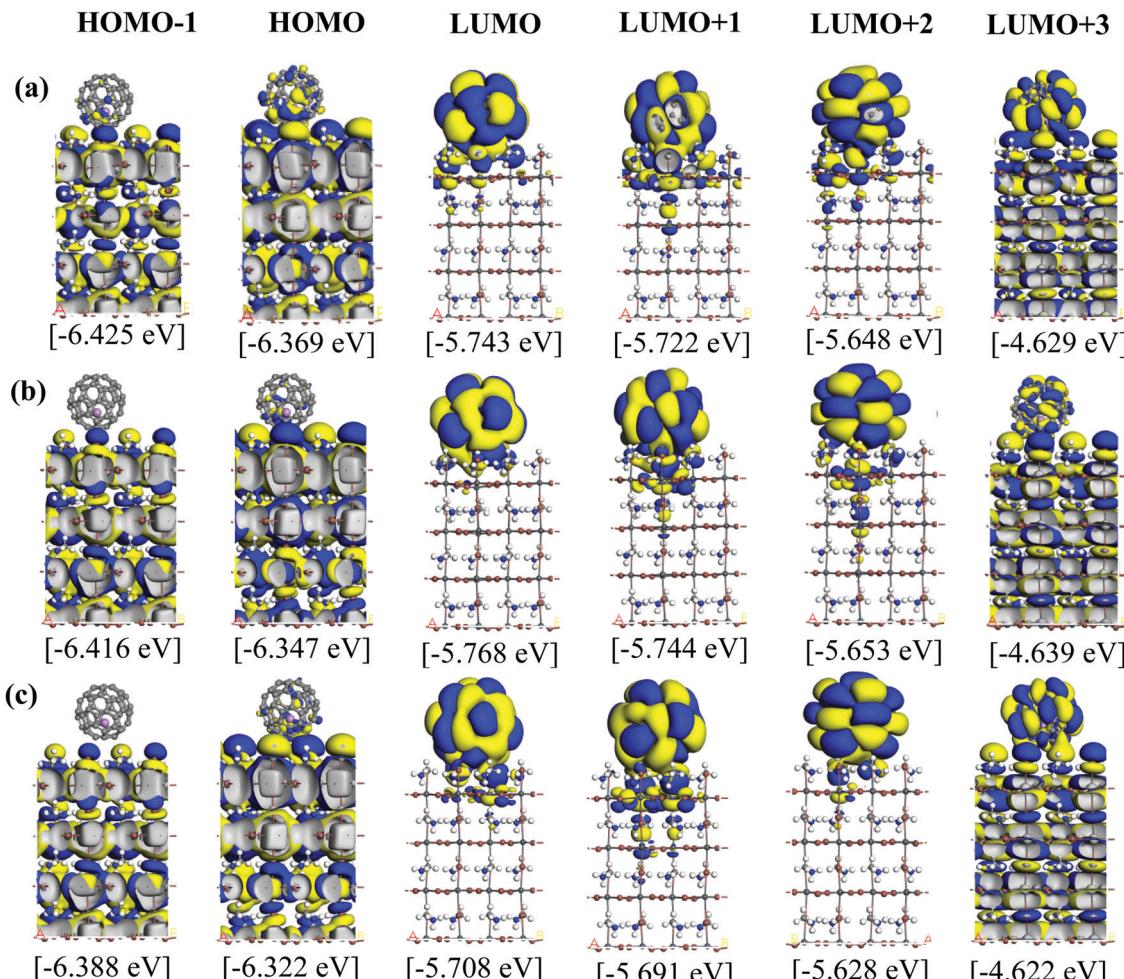
Fig. 6 Calculated KS orbitals and energy eigenvalues of $MAPbI_3/Li^+@C_{60}$ from the HOMO−1 to LUMO+3 levels. The Li^+ located at the off-central bottom inside the C_{60} cage. Yellow and blue denote the plus and minus regions of the orbitals. The perovskite has a topC orientation with $Li^+@C_{60}$ on the (a) aboveC, (b) aboveI and (c) bridge positions.

a neutral lithium endohedral fullerene $Li@C_{60}$ absorbed on the aboveC geometry of $MAPbI_3$. In Table 2, we summarize the atomic distance of selected atoms/molecules (fragments) located at the $MAPbI_3/Li^+@C_{60}$ interface, as well as the $MAPbI_3/Li@C_{60}$ interface. A more comprehensive analysis of results can be found in Fig. S4–S11 in the ESI.†

In the following, we correlate the findings in Table 2 with the stability (Fig. 2(a)) and the binding energy (Fig. 3) of the $MAPbI_3/Li^+@C_{60}$ system. From Fig. 2(a), we found that the energetically most stable geometry of the $MAPbI_3/Li^+@C_{60}$ system is the aboveC geometry and the next stable geometry is the aboveI position. However, both the aboveC and bridge geometries have the $C\cdots H(-C)$, $C\cdots C(-H)$ and $C\cdots I(-Pb)$ interactions. The results from Table 2 show that the main difference between these two geometries is the $C\cdots H(-C)$ atomic distance: the aboveC geometry is in the ranges of 2.612–2.660 Å, whereas it is in the range of 2.791–2.990 Å for the aboveI geometry. This suggests that the $C\cdots H(-C)$ interaction, i.e. the π–CH interaction, plays a crucial role in governing the stability of the $MAPbI_3/Li^+@C_{60}$ system and the strength of binding between

the $MAPbI_3$ and $Li^+@C_{60}$. The $MAPbI_3/Li^+@C_{60}$ system with the aboveI geometry is the least stable structure among the three geometries (though they have six $C\cdots I(-Pb)$ interactions with highly electronegative iodines), implying that the $C\cdots I(-Pb)$ interactions, i.e. the π–I interaction, contributed less as compared with the $C\cdots H(-C)$ interactions. All the atomic distances $C\cdots H(-C)$, $C\cdots C(-H)$ and $C\cdots I(-Pb)$ of the $MAPbI_3/Li^+(bottom)@C_{60}$ system are shorter than those of the $MAPbI_3/Li^+(top)@C_{60}$ system. Therefore, the $MAPbI_3/Li^+(bottom)@C_{60}$ system is energetically more stable than the $MAPbI_3/Li^+(top)@C_{60}$ system for the structure with the same geometry (Fig. 2(a)). For the same geometry, the binding energy of the $MAPbI_3/Li^+(bottom)@C_{60}$ system is also stronger than that of the $MAPbI_3/Li^+(top)@C_{60}$ system. Although the $MAPbI_3/Li@C_{60}$ system has a weak binding energy (Fig. 3), both the $MAPbI_3/Li(top)@C_{60}$ system and the $MAPbI_3/Li(bottom)@C_{60}$ system have six bond distances within the vdW interactions (Fig. S4 and S5, ESI†), i.e. three $C\cdots H(-C)$ in the range 2.618–2.673 Å, two $C\cdots C(-H)$ in the range 3.538–3.547 Å, and one $C\cdots I(-Pb)$ in the range 3.744–3.782 Å, with a small energy difference of

HOMO-5 (+ spin)	HOMO-4 (- spin)	HOMO-3 (+ spin)	HOMO-2 (- spin)	HOMO-1 (+ spin)	HOMO (SOMO, - spin)
[-5.679 eV]	[-5.666 eV]	[-5.666 eV]	[-5.603 eV]	[-5.603 eV]	[-5.127 eV]

| LUMO (+ spin)	LUMO+1 (- spin)	LUMO+2 (+ spin)	LUMO+3 (- spin)	LUMO+4 (+ spin)	LUMO+5 (- spin)
[-5.002 eV]	[-4.989 eV]	[-4.962 eV]	[-4.939 eV]	[-4.911 eV]	[-3.979 eV]
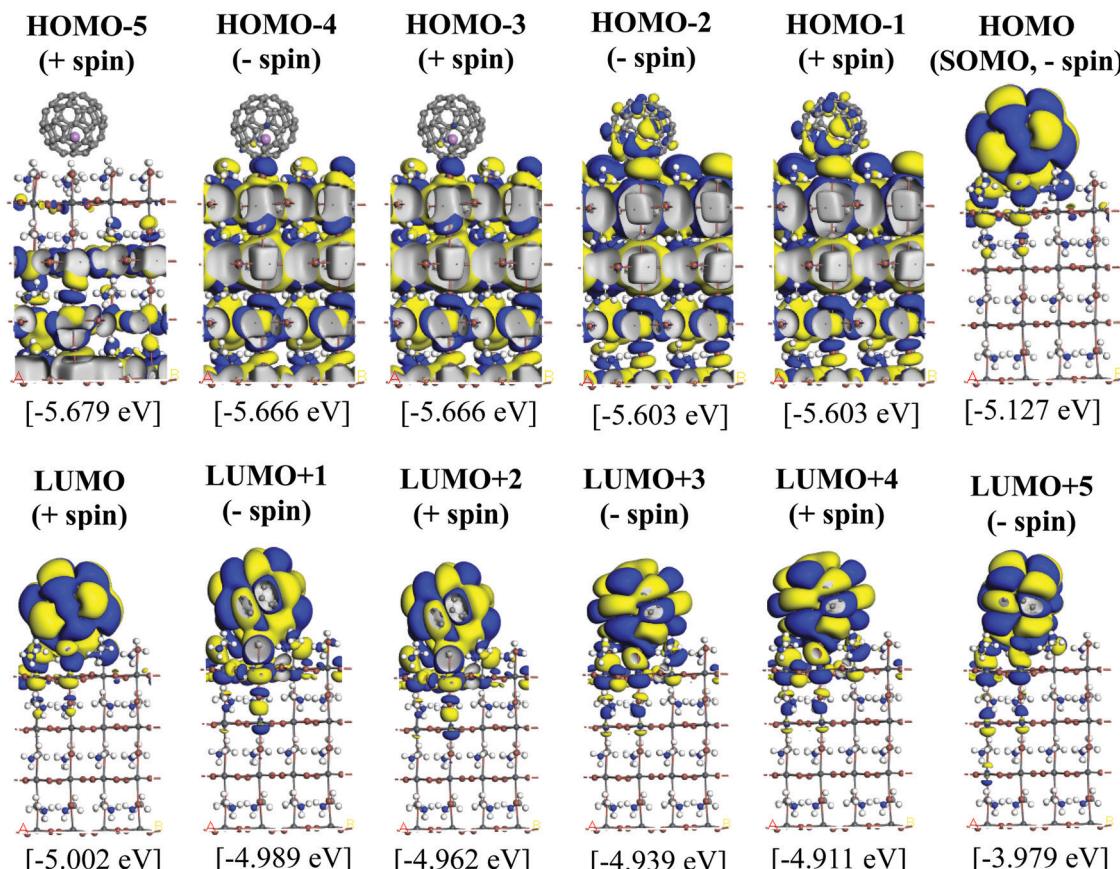
Fig. 7 Calculated KS orbitals and energy eigenvalues of a perovskite $MAPbI_3$ with a neutral lithium endohedral fullerene $Li@C_{60}$ on the aboveC position. The Li is located at the off-central bottom inside the C_{60} cage. Yellow and blue denote the plus and minus regions of the orbitals.

~ 0.008 eV (Fig. 2(a)). The stability of the $Li@C_{60}$ molecule is another important factor that contributes to the strength of binding between the $MAPbI_3$ perovskite and the $Li@C_{60}$ molecule, besides the atomic distances at the $MAPbI_3/Li^+@C_{60}$ interface. Although this simple analysis may provide a rough picture of the interaction at the $MAPbI_3/Li^+@C_{60}$ (or $Li@C_{60}$) interface, it is important to note that the calculated atomic distances using the GGA-PBE may not be accurate. In addition, the lattice dynamics play an important role in determining the structural and electronic properties of these halide perovskites,[54–56] and the tetragonal structure of $MAPbI_3$ perovskite at room temperature is strongly anharmonic.[57]

After gaining an understanding of the correlation between the stability and the vdW interactions at the interface, we investigated the atomic charge distribution at the interface between the $MAPbI_3$ perovskite and $Li^+@C_{60}$ (or $Li@ C_{60}$). We performed an atomic charge analysis using the geometrical optimized structure of the $MAPbI_3/Li^+@C_{60}$ (and $MAPbI_3/Li@C_{60}$) system. We employed the Hirshfeld atomic population analysis, which is based on the electron density at individual atoms.[58,59] The Hirshfeld charges of an individual $Li@C_{60}$ molecule and the $MAPbI_3$ slab are $0.0e$ and $-0.005e$, respectively, indicating that they possess neutral charges. On the other hand, the calculated Hirshfeld charge of the individual

$Li^+@C_{60}$ molecule was $0.998e$, $\sim +1e$, as expected. Table 3 summarizes the Hirshfeld atomic charges of selected fragments $[CH_3]$ and $[I]$ at the $MAPbI_3/Li^+@C_{60}$ interface. Q is the charge transferred from $[MAPbI_3]$ to $[Li^+@C_{60}]$. $[Li^+@C_{60}]$ and $[MAPbI_3]$ denote the calculated Hirshfeld fragments of the $MAPbI_3/Li^+@C_{60}$ system. Calculated Hirshfeld atomic charges of a $MAPbI_3$ with a neutral lithium endohedral fullerene $Li@C_{60}$ are for only the aboveC position. A more detailed analysis of the Hirshfeld atomic charges of fragments $[CH_3]$, $[I]$, $[Li]$, $[Li^+]$, and $[C]$ at the $MAPbI_3/Li^+@C_{60}$ interface with the $Li^+@C_{60}$ can be found in Table S2 of the ESI.† From Table 3, the $MAPbI_3/Li@C_{60}$ system also possesses a neutral charge similar to the Hirshfeld charge of the individual $Li@C_{60}$ molecule and the $MAPbI_3$ slab, as expected. For the $MAPbI_3/Li^+@C_{60}$ system, the calculated Hirshfeld charge for all three geometries including the Li^+ located at the off-central top and bottom positions inside the C_{60} cage is $\sim +1.0e$, which is the same as the isolated $Li^+@C_{60}$ molecule. In the $MAPbI_3/Li^+@C_{60}$ system, the amount of charge transfer Q from the $MAPbI_3$ to $Li^+@C_{60}$ increased in the order of bridge > aboveI > aboveC geometry. The most stable $MAPbI_3/Li@C_{60}$ system with the aboveC geometry has the highest amount of charge transfer Q, therefore possessing the strongest binding energy. However, the amount of charge transfer of the $MAPbI_3/Li^+@C_{60}$ system with the aboveI position
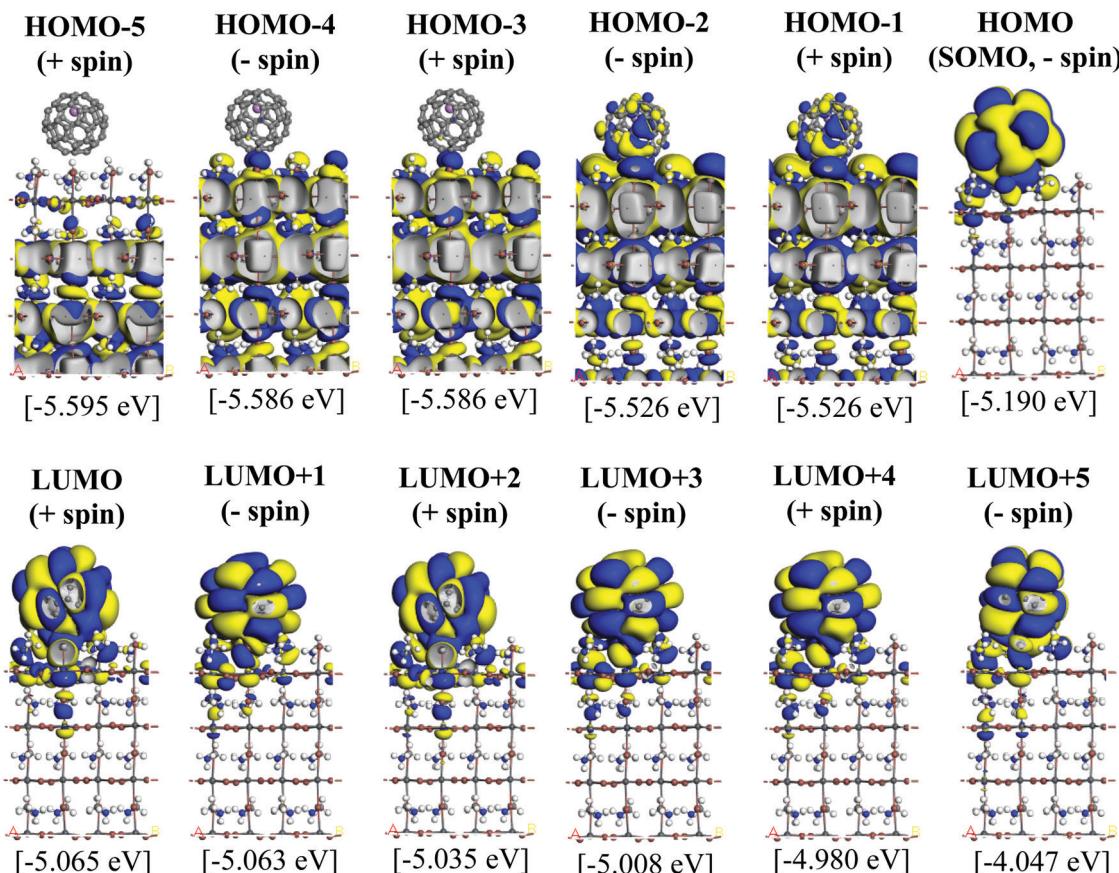
Fig. 8 Calculated KS orbitals and energy eigenvalues of a perovskite $MAPbI_3$ with a neutral lithium endohedral fullerene $Li@C_{60}$ on the aboveC position. The Li is located at the off-central top inside the C_{60} cage. Yellow and blue denote the plus and minus regions of the orbitals.

is higher than that of the $MAPbI_3/Li^+@C_{60}$ system with the bridge position, though the system with the aboveI position is more stable and possesses stronger binding energy. This is because the charge transfer of $MAPbI_3$ to the $Li^+@C_{60}$ on the aboveI position is facilitated by the iodine, which has a high electronegativity. This was evidenced by the fragment [I1] of the aboveI geometry possessing Hirshfeld charges of $-0.169e$ to $-0.177e$, whereas fragment [I1] of the aboveC and bridge geometries have the Hirshfeld charges of $> -0.2e$. This implies that more charges are transferred by fragment [I1] in the $MAPbI_3/Li^+@C_{60}$ system with the aboveI position than that of the system with the aboveC or bridge position. Since the $MAPbI_3/Li@C_{60}$ system is neutral, there is almost no transfer of charge $Q \sim 0e$.

Fig. 5 and 6 illustrate the Kohn–Sham (KS) orbitals and energy eigenvalues of the topC heterojunction with a $Li^+@C_{60}$ on the aboveC, aboveI, and bridge positions for Li^+ located at the off-central top and bottom inside the C_{60} cage, respectively. From the KS orbitals and energy eigenvalues, we find that the energy gap of $MAPbI_3$ is between the HOMO and LUMO+3 levels and amounts to 1.6–1.7 eV. Under light illumination, electrons are excited by this energy and transferred to the ETM, then holes are produced at the HOMO and HOMO−1 levels in the HTM. If there is no other level in the wide band gap of

$MAPbI_3$, the created holes can promote the following reactions, similar to the case of TiO_2:[60]

$$MAPbI_3 \ (h^+) + H_2O \rightarrow MAPbI_3 + HO^\bullet + H^+ \quad (1a)$$

$$MAPbI_3 \ (h^+) + OH^- \rightarrow MAPbI_3 + HO^\bullet \quad (1b)$$

Inside the band gap of $MAPbI_3$, however, the LUMO, LUMO+1, and LUMO+2 levels are localized at $Li^+@C_{60}$. The location of these levels is about 0.6 eV higher than the HOMO level (see also Table S1, ESI†). These levels reflect the situation after an electron is transferred from $Li@C_{60}$ to infinitely far away, and a hole is created in the system. The KS energy levels of the neutral, spin-polarized $MAPbI_3/Li@C_{60}$ system (before an electron is transferred from $Li@C_{60}$) are shown in Fig. 7 and 8, respectively, for the off-central bottom and top Li positions. The neutral $Li@C_{60}$ in this system may be regarded as $Li^+@C_{60}^{\bullet-}$ in ref. 61. The HOMO (SOMO, – spin) and LUMO (+spin) levels are localized at $Li@C_{60}$, and the latter is higher than the former by 0.125 eV; see also the values in the parentheses in Table 2. This is much smaller than the energy difference (0.336 eV for top Li position and 0.476 eV for bottom Li position) between the HOMO (SOMO, – spin) and HOMO−1 (+spin) levels. Therefore, the hole can easily migrate between $Li@C_{60}$ molecules, not deep inside the $MAPbI_3$. This is a critical reason why the hole

does not directly attack the MAPbI$_3$ surface when Li$^+$@C$_{60}$ exists on the surface.

Conclusions

In summary, we have performed first-principles DFT calculations on the electronic structure of MAPbI$_3$/Li$^+$@C$_{60}$ heterojunctions. Finite slab models of tetragonal MAPbI$_3$ (001) surfaces with MAI terminations were considered. A Li$^+$ (or Li) endohedral fullerene Li$^+$@C$_{60}$ (or Li@C$_{60}$) was introduced at different positions on the MAPbI$_3$ surface. We considered the energetically most stable topC geometry of the tetragonal MAPbI3 surface and found that the Li$^+$@C$_{60}$ was adsorbed at the aboveC position with almost 100% ionization. There was not much difference between the top and bottom positions of Li$^+$ inside C$_{60}$, but the bottom position was slightly more stable than the top position. In the MAPbI3/Li$^+$@C$_{60}$ system, the KS wave functions of the HOMO and HOMO−1 levels were spread out in MAPbI3 and those of the LUMO, LUMO+1, LUMO+2 levels were localized in Li$^+$@C$_{60}$; the energy gap between these levels was 0.6 eV. Thus, in the neutral, spin-polarized MAPbI$_3$/Li@C$_{60}$ system, the KS wave functions of the HOMO (SOMO, −spin) and LUMO (+spin) levels were both localized in Li@C$_{60}$ and their energy gap of 0.125 eV was very small. This HOMO (SOMO) level behaves as a hole level when it loses an electron to become Li$^+$@C$_{60}$. Since there were three almost degenerate LUMO+1 and LUMO+2 levels, it was expected to behave as a good hole conductor. Due to this fact, we concluded that the use of Li$^+$@C$_{60}$ molecules in place of the bare Li-ions as dopant materials in the MAPbI$_3$ solar cells can prevent degradation. In any case, regardless of the adsorption geometry, our results clearly show the existence of the energetically isolated hole level localized in the Li@C$_{60}$, which may successfully contribute to the suppression of the oxidation of the MAPbI$_3$ surface. Thus, the present study reveals the stability of the MAPbI$_3$ surfaces.

Conflicts of interest

There are no conflicts to declare.

Acknowledgements

References

1 A. Kojima, K. Teshima, Y. Shirai and T. Miyasaka, *J. Am. Chem. Soc.*, 2009, **131**, 6050.

2 M. M. Lee, J. Teuscher, T. Miyasaka, T. N. Murakami and H. J. Snaith, *Science*, 2012, **338**, 643.

3 A. K. Jena, A. Kulkarmi and T. Miyasaka, *Chem. Rev.*, 2019, **119**, 3036.

4 X. Li, D. Bi, C. Yi, J.-D. Decoppet, J. Luo, S. M. Zakeeruddin, A. Hagfeldt and M. A. Gratzel, *Science*, 2016, **353**, 58.

5 N. J. Jeon, H. Na, E. H. Jung, T.-Y. Yang, Y. G. Lee, G. Kim, H. W. Shin, S. I. Seok, J. Lee and J. Seo, *Nat. Energy*, 2018, **3**, 682.

6 A. Y. Alsalloum, B. Turedi, X. Zheng, S. Mitra, A. A. Zhumekenov, K. J. Lee, P. Maity, I. Gereige, A. AlSaggaf, I. S. Roqan, O. F. Mohammed and O. M. Bakr, *ACS Energy Lett.*, 2020, **5**, 657.

7 K.-H. Chew, R. Kuwahara and K. Ohno, *Mater. Adv.*, 2021, **2**, 1665.

8 Y. Fang, C. Bi, D. Wang and J. Huang, *ACS Energy Lett.*, 2017, **2**, 782.

9 T. Gatti, E. Menna, M. Meneghetti, M. Maggini, A. Petrozza and F. Lamberti, *Nano Energy*, 2017, **41**, 84.

10 J. Pascual, J. L. Delgado and R. Tena-Zaera, *J. Phys. Chem. Lett.*, 2018, **9**, 2893.

11 E. Castro, J. Murillo, O. Fernandez-Delgado and L. Echegoyen, *J. Mater. Chem. C*, 2018, **6**, 2635.

12 H.-S. Kim, C.-R. Lee, J.-H. Im, K.-B. Lee, T. Moehl, A. Marchioro, S.-J. Moon, H.-B. Robin, J.-H. Yum, J. E. Moser, M. Grätzel and N.-G. Park, *Sci. Rep.*, 2012, **2**, 591.

13 J. Liu, Y. Wu, C. Qin, X. Yang, T. Yasuda, A. Islam, K. Zhang, W. Peng, W. Chena and L. Han, *Energy Environ. Sci.*, 2014, **7**, 2963.

14 R. S. Sanchez and E. Mas-Marza, *Solar Energy Mater., Solar Cells*, 2016, **158**, 189.

15 F. Zhao, L. Deng, K. Wang, C. Han, Z. Liu, H. Yu, J. Li and B. Hu, *Appl. Mater. Interfaces*, 2020, **12**, 5120.

16 K. Domanski, J.-P. Correa-Baena, N. Mine, M. K. Nazeeruddin, A. Abate, M. Saliba, W. Tress, A. Hagfeldt and M. Grätzel, *ACS Nano*, 2016, **10**, 6306.

17 A. K. Jena, Y. Numata, M. Ikegami and T. Miyasaka, *J. Mater. Chem. A*, 2018, **6**, 2219.

18 I. Jeon, H. Ueno, S. Seo, K. Aitola, R. Nishikubo, A. Saeki, H. Okada, G. Boschloo, S. Maruyama and Y. Matsuo, *Angew. Chem.*, 2018, **57**, 4607.

19 S. Yun, X. Zhou, J. Even and A. Hagfeldt, *Angew. Chem., Int. Ed.*, 2017, **56**, 15806.

20 X. Zhou, J. Jankowska, H. Dong and O. V. Prezhdo, *J. Energy Chem.*, 2018, **27**, 637.

21 C.-J. Yu, *J. Phys. Energy*, 2019, **1**, 022001.

22 J. Yin, D. Cortecchia, A. Krishna, S. Chen, N. Mathews, A. C. Grimsdale and C. Soci, *J. Phys. Chem. Lett.*, 2015, **6**, 1396.

23 S. Aoyagi, E. Nishibori, H. Sawa, K. Sugimoto, M. Takata, Y. Miyata, R. Kitaura, H. Shinohara, H. Okada, T. Sakai, Y. Ono, K. Kawachi, K. Yokoo, S. Ono, K. Omote, Y. Kasama, S. Ishikawa, T. Komuro and H. Tobita, *Nat. Chem.*, 2010, **2**, 678.

24 K. Ohno, Y. Maruyama, K. Esfarjani, Y. Kawazoe, N. Sato, R. Hatakeyama, T. Hirata and M. Niwano, *Phys. Rev. Lett.*, 1996, **76**, 3590.

25 E. E. B. Campbell, R. Tellgmann, N. Krawez and I. V. Hertel, *J. Phys. Chem. Solids*, 1997, **58**, 1763.

26 R. Hatakeyama, *Rev. Mod. Plasma Phys.*, 2017, **1**, 7.

27 K. Ohno, A. Manjanath, Y. Kawazoe, R. Hatakeyama, F. Misaizu, E. Kwon, H. Fukumura, H. Ogasawara, Y. Yamada, C. Zhang, N. Sumi, T. Kamigak, K. Kawachi, K. Yokoo, S. Ono, Y. Kasama, K. Ohno, A. Manjanath, Y. Kawazoe, R. Hatakeyama, F. Misaizu, E. Kwon, H. Fukumura, H. Ogasawara, Y. Yamada, C. Zhang, N. Sumi, T. Kamigak, K. Kawachi, K. Yokoo, S. Ono and Y. Kasama, *Nanoscale*, 2018, **10**, 1825.

28 H. Ueno, K. Kokubo, Y. Nakamura, K. Ohkubo, N. Ikuma, H. Moriyama, S. Fukuzumi and T. Oshima, *Chem. Commun.*, 2013, **49**, 7376.

29 Y. Kawashima, K. Ohkubo and S. Fukuzumi, *Chem. – Asian J.*, 2015, **10**, 44.

30 Y. Yamada, A. V. Kuklin, S. Sato, F. Esaka, N. Sumi, C. Zhang, M. Sasaki, E. Kwon, Y. Kasama, P. V. Avramov and S. Sakai, *Carbon*, 2018, **133**, 23.

31 H. J. Chandler, M. Stefanou, E. E. B. Campbell and R. Schaub, *Nat. Commun.*, 2019, **10**, 2283.

32 K. Miwa, S. Aoyagi, T. Sasamori, H. Ueno, H. Okada and K. Ohkubo, *J. Phys. Chem. B*, 2021, **125**, 918.

33 H. Ando and Y. Nakao, *Phys. Chem. Chem. Phys.*, 2021, **23**, 9785.

34 B. Delley, *J. Chem. Phys.*, 1990, **92**, 508.

35 B. Delley, *J. Chem. Phys.*, 2000, **113**, 7756.

36 B. Delley, in *Modern density functional theory: A tool for chemistry in theoretical and computational chemistry*. ed. J. M. Seminario and P. Politzer, Elservier, 1995, Vol. 2.

37 E. R. McNellis, J. Meyer and K. Reuter, *Phys. Rev. B: Condens. Matter Mater. Phys.*, 2009, **80**, 205414.

38 A. Tkatchenko and M. Scheffler, *Phys. Rev. Lett.*, 2009, **102**, 073005.

39 J. P. Perdew, K. Burke and M. Ernzerhof, *Phys. Rev. Lett.*, 1996, **77**, 3865.

40 W.-J. Yin, T. Shi and Y. Yan, *J. Phys. Chem. C*, 2015, **119**, 5253.

41 R. A. Jishi, O. B. Ta and A. A. Sharif, *J. Phys. Chem. C*, 2014, **118**, 28344.

42 W. Geng, L. Zhang, Y.-N. Zhang, W.-M. Lau and L.-M. Liu, *J. Phys. Chem. C*, 2014, **118**, 19565.

43 A. Poglitsch and D. Weber, *J. Chem. Phys.*, 1987, **87**, 6373.

44 Y. Kawamura, H. Mashiyama and K. Hasebe, *J. Phys. Soc. Jpn.*, 2002, **71**, 1694.

45 C. Quarti, F. De Angelis and D. Beljonne, *Chem. Mater.*, 2017, **29**, 958.

46 J. Järvi, J. Li and P. Rinke, *New J. Phys.*, 2018, **20**, 103013.

47 M. Wierzbowska, J. J. Melendez and D. Varsano, *Comput. Mater. Sci.*, 2018, **142**, 361.

48 C. Motta, F. El-Mellouhi, S. Kais, N. Tabet, F. Alharabi and S. Sanvito, *Nat. Commun.*, 2015, **6**, 7026.

49 V. D'Innocenzo, G. Grancini, M. J. P. Alcocer, A. R. S. Kandada, S. D. Stranks, M. M. Lee, G. Lanzani, H. J. Snaith and A. Petrozza, *Nat. Commun.*, 2014, **5**, 3586.

50 S. Kawai, T. Nishiuchi, T. Kodama, P. Spijker, R. Pawlak, T. Meier, J. Tracey, T. Kubo, E. Meyer and A. D. Foster, *Sci. Adv.*, 2017, **3**, e1603258.

51 Z. Han, G. Czap, C.-I. Chiang, C. Xu, P. J. Wagner, X. Wei, Y. Zhang, R. Wu and W. Ho, *Science*, 2017, **358**, 206.

52 S. Kawai, A. Sadeghi, F. Xu, L. Peng, A. Orita, J. Otera, S. Goedecker and E. Meyer, *ACS Nano*, 2015, **9**, 2574.

53 S. Alvarez, *Dalton Trans.*, 2013, **42**, 8617.

54 F. Brivio, J. M. Frost, J. M. Skelton, A. J. Jackson, O. J. Weber, M. T. Weller, A. R. Goñi, A. M. A. Leguy, P. R. F. Barnes and A. Walsh, *Phys. Rev. B: Condens. Matter Mater. Phys.*, 2015, **92**, 144308.

55 M. Grechko, S. A. Bretschneider, L. Vietze, H. Kim and M. Bonn, *Angew. Chem., Int. Ed.*, 2018, **57**, 13657.

56 K. N. Boldyrev, V. E. Anikeeva, O. I. Semenova and M. N. Popova, *J. Phys. Chem. C*, 2020, **124**, 23307.

57 R. Sharma, Z. Dai, L. Gao, T. M. Brenner, L. Yadgarov, J. Zhang, Y. Rakita, R. Korobko, A. M. Rappe and O. Yaffe, *Phys. Rev. Mater.*, 2020, **4**, 092401(R).

58 V. Siva, A. Shameem, A. Murugan, S. Athimoolam, M. Suresh and S. A. Bahadur, *Chem. Data Collect.*, 2019, **24**, 100281.

59 F. L. Hirshfeld, *Theor. Chim. Acta*, 1977, **44**, 129.

60 O. Legrini, E. Oliveros and A. M. Braun, *Chem. Rev.*, 1993, **93**, 671.

61 H. Okada, H. Ueno, Y. Takabayashi, T. Nakagawa, M. Vrankić, J. Arvanitidis, T. Kusamoto, K. Prassides and Y. Matsuo, *Carbon*, 2019, **153**, 467.